

# DNS investigation of the flow induced by an unsteady wall injection

F. Chedevergne, G. Casalis

*ONERA, Fundamental and Applied Energetics Department,  
29 av. de la Division Leclerc BP 72, 92320 Chatillon Cedex , FRANCE.  
email : francois.chedevergne@onera.fr*

## ABSTRACT

In this article, we use a linear biglobal stability approach to identify the intrinsic instability modes that are responsible for triggering large thrust oscillations in long segmented solid rocket motors. Corresponding theoretical predictions compare very favorably with existing experimental measurements acquired from subscale motors tests and cold gas experiments. Specifically, the frequency signatures of the thrust oscillations, which form distinct frequency paths, are found to be directly connected to the emergence of the intrinsic instabilities of the flow. When these are coupled with the natural acoustic modes of the chamber, large amplitude oscillations are triggered. After undergoing spatial amplification, these oscillations depreciate with the passage of time. To further understand the results obtained from theory, DNS calculations of the rocket motor are performed. These simulations provide evidences of the existence of a coupling mechanism between acoustic modes and eigenmodes. This gives rise to a new physical understanding of the thrust oscillations phenomenon.

## 1 INTRODUCTION

FOR several years, thrust oscillations which occur in solid rocket motors, especially in the P230, have been extensively studied thanks to different approaches. One can distinguish three main kind of approaches. First, experiments, based on subscale solid rocket motors or cold gas facilities, have provided a detailed data base which can be used for validating models. Moreover, simple test cases led to the identification of a particular phenomenon, called VSP (acronym for Parietal Vortex Shedding), which is suspected to be responsible of the arising of the thrust oscillations. The second approach is based on numerical simulation. In spite of the fact that the numerical reproduction of the thrust oscillations seem to be out of reach, some contributors have performed simulations in which VSP exist, thus confirming the measurements. The last approaches used to study the thrust oscillations rely on theoretical models such as perturbation calculations. In particular, recent developments [1], involving the biglobal linear stability analysis, have

given a new insight upon the thrust oscillations phenomenon. Thanks to this approach, the frequency signature of the thrust oscillations, characterized by frequency paths, can be well predicted. In addition, successful comparisons [2] with subscale solid rocket motors measurements [3] have proved the relevance of this theory. Likewise, cold gas experiments, conducted by G. Avalon [4], which provide a large amount of data in a configuration close to the theoretical model, have also led to very good agreement.

Thanks to these results, a new understanding of the thrust oscillations arising has been revealed. In particular, the intrinsic modes of the flow, highlighted by the linear stability theory, are believed to be coupled to the acoustic modes of the motor. To further investigate this possible coupling mechanism, DNS have been performed with the use of the ONERA code CEDRE.

This paper is organized as follows. First, the basis of the linear stability theory will be given. Then, the numerical procedure for the DNS calculations will be explained. Finally, the last part will dis-

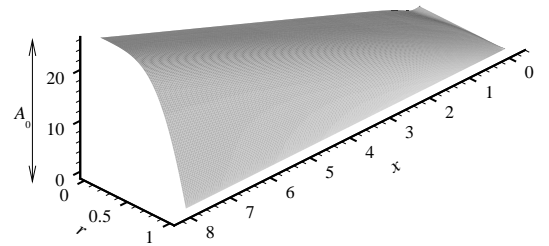
cuss the results and in the conclusion the basis of a scenario leading to the triggering of the thrust oscillation will be exposed.

## 2 BIGLOBAL LINEAR STABILITY ANALYSIS

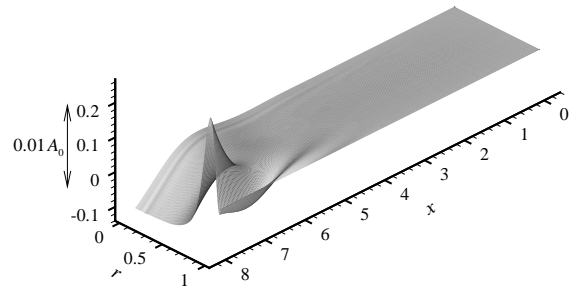
### 2.1 Mean Flow Model

First we select a model flow to represent the steady-state profile established in a solid rocket motor. The simulated geometry corresponds to a semi-infinite cylinder of radius  $R$ . A steady, incompressible fluid is injected through the sidewall at a constant and spatially uniform velocity  $V_{inj}$ . The flow enters in the radial direction  $r$ , thus simulating the gas ejection at the burning surface of the propellant. The spatial coordinates and the velocities are made dimensionless with respect to the radius  $R$  and the wall-injection velocity  $V_{inj}$ . Although the Taylor-Culick model corresponds to a semi-infinite cylinder, ours is truncated at  $x = X_e$ , thus forming a finite chamber that can be practically simulated using a computational code named CEDRE (*Calcul d'Écoulements Diphasiques Réactifs pour l'Énergétique*). This code is developed at ONERA to serve multiple functions, including the calculation of the mean flow field in a user-designated solid rocket motor chamber. CEDRE incorporates innovative techniques, such as the generalized unstructured approach, to offer a unique computational platform for simulating complex problems with reactive multiphysics. More details on the computations can be found in subsection 3.1.

Figures 1(a) and 2(a) provide three-dimensional views of the mean axial and radial velocity components computed at a dimensionless  $X_e = 8$  and  $V_{inj} = 1$  m/s. One notes that this flow closely resembles the Taylor-Culick model [5, 6] except in the fore-end region where a boundary layer develops in fulfilment of the no-slip requirement at the headwall (see [7]). The CEDRE-based solution is computed in the  $(x, r)$  plane assuming axisymmetric, rotational, laminar flow. The agreement obtained between the computed flow and the Taylor-Culick profile confirms the essentially incompressible character of the flow. While a compressible solution for the Taylor-Culick problem has been recently developed by [8], it is not employed here due to the relatively small velocities characterizing our problem. Furthermore, experimental measurements obtained through ONERA's cold gas facility

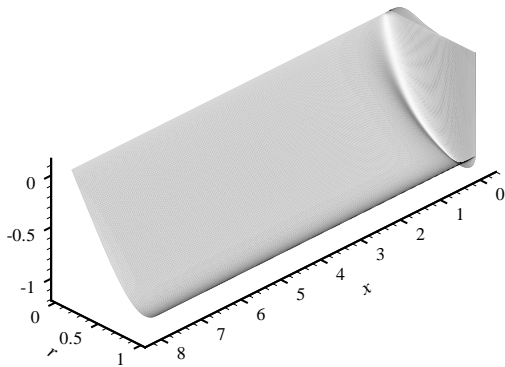


(a)  $\bar{U}_x$

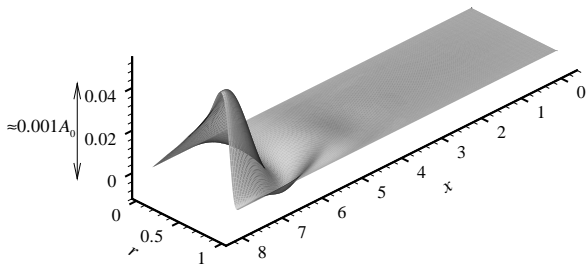


(b)  $(\hat{u}_x)_r$

Figure 1: Longitudinal components of the velocities of the basic flow  $\bar{U}_x$  and of the perturbation  $\hat{u}_x$  (real part). Here the initial amplitude  $A$  and time  $t$  of (3) are  $t = 0$  and  $A = 0.01A_0$ .



(a)  $\bar{U}_r$



(b)  $(\hat{u}_r)_r$

Figure 2: Radial components of the velocities of the basic flow  $\bar{U}_r$  and of the perturbation  $\hat{u}_r$  (real part).

VALDO [4] provide an additional avenue for validation, being in agreement with our model. Note that VALDO uses a cylindrical chamber of radius  $R_0 = 0.03$  m made of poral (bronze porous material), thus providing the possibility to vary  $V_{inj}$  from 0.6 m/s up to 2 m/s. The length of the chamber  $X_e$  in VALDO can also vary from  $11.2R_0$  to  $22.4R_0$ . Thus, the injection-based Reynolds number, defined as usual by  $Re = \rho R V_{inj} / \mu$ , ranges between 1,200 and 4,000 in the VALDO facility. Note that the Reynolds number is the only group parameter that remains in the Navier-Stokes equations.

## 2.2 Biglobal Fluctuations

The stability analysis is based on a perturbation technique that considers any physical quantity  $Q$  to be a superposition of a mean (steady) variable  $\bar{Q}$  and a fluctuating, time-dependent part  $q$ . If solutions exist for  $q$ , they will be called intrinsic instabilities of the mean flow. The decomposition  $Q = \bar{Q} + q$  is introduced into the Navier-Stokes equations which, after some simplifications and cancellations, are split into a linear system of partial differential equations (PDEs). These PDEs prescribe the motion of time-dependent disturbances  $q$ . In the linearized system, the mean flow and its derivatives define the main coefficients. Next, the biglobal instability theory is applied. Accordingly, any perturbation  $q$  may be judiciously expressed as :

$$q = \hat{q}(x, r) e^{i(n\theta - \omega t)} \quad (1)$$

This unsteady variable representation is consistent with the mean flow being dependent on both  $x$  and  $r$ . It is spatially more accurate than one-dimensional approximations in which  $\hat{q}$  is taken to be a function of the radial coordinate only. In equation (1),  $n$  is an integer that denotes the azimuthal wave number, an index that vanishes for strictly axisymmetric disturbances,  $\theta$  stands for the azimuthal angle, and  $\omega$  represents the complex circular frequency. While its real part  $\omega_r$  reproduces the circular frequency of oscillations, its imaginary part  $\omega_i$  controls the temporal growth rate.

As we take a first look at this problem, we focus our attention on the axisymmetric models for which  $n = 0$ . This case is not restrictive because higher tangential modes tend to be less critical from a stability standpoint.

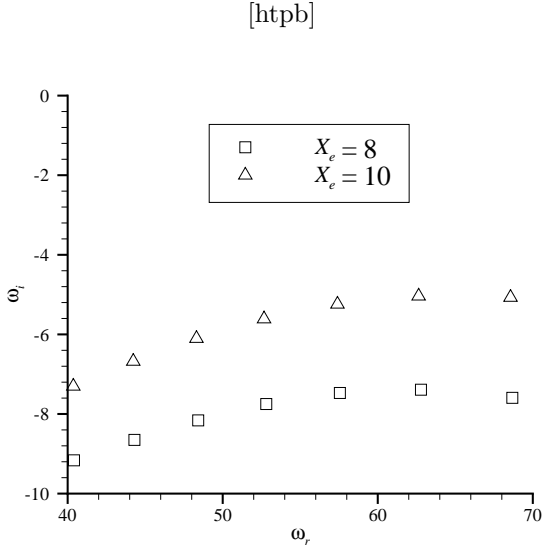


Figure 3: Set of eigenvalues in the complex  $(\omega_r, \omega_i)$  plane for  $Re = 1975$ . Two cases are shown :  $X_e = 8$  (squares) and  $X_e = 10$  (triangles).

### 2.3 Stability Identification Procedure

The use of  $n = 0$  enables us to define a stream function  $\psi$  for the perturbation. In fact, the linearized Navier-Stokes equations written for the stream function  $\psi$  lead to a fourth order PDE ( $E$ ) in  $(x, r)$ . This equation can then be solved for  $(x, r) \in [0, X_e] \times [0, 1]$ . As boundary conditions are imposed on the stream function, a suitable outflow condition is formulated at  $x = X_e$  following [9] and [10]. After discretization in the computational domain, ( $E$ ) is written as a generalized eigenvalue problem  $\underline{A} \underline{\Psi} = \omega \underline{B} \underline{\Psi}$ . Then, Arnoldi's algorithm is implemented to the extent of generating both problem's complex eigenvalues  $\omega$  and their associated eigenfunctions [11]. The set of complex eigenvalues  $\omega$  defines the spectrum of the stability problem. In the interest of clarity, a sample set of complex eigenvalues is showcased in figure 3 for  $Re = 1975$ . It should be noted that for each calculated eigenvalue  $\omega$  in figure 3, a companion eigenvector  $\underline{\Psi}$  is obtained with its components representing the discretized values of the associated eigenfunction  $\hat{\psi}(x, r)$ . In relation to axial and radial velocity eigenfunctions, one has :

$$\hat{u}_x = \frac{1}{r} \frac{\partial \hat{\psi}}{\partial r} \quad \text{and} \quad \hat{u}_r = -\frac{1}{r} \frac{\partial \hat{\psi}}{\partial x} \quad (2)$$

The perturbation  $q = \hat{q}e^{-i\omega t}$  will therefore contain the essential fluctuating flow ingredients such

as  $u_x, u_r, p$  and their derivatives; it is referred to as an instability mode, being different for each  $\omega$ . Once the results of the stability analysis are recast into dimensional quantities (using the constant parameters  $R$  and  $V_{inj}$ ), a physical perturbation  $q$  for a given mode  $\omega = \omega^0$  can be written as :

$$\begin{aligned} q &= A \hat{q} e^{i \frac{V_{inj}}{R} \omega^0 t} \\ &= A [(\hat{q})_r \cos(2\pi f t) + (\hat{q})_i \sin(2\pi f t)] e^{\nu t} \\ &\text{with } f = \frac{V_{inj}}{2\pi R} \omega_r^0 \quad \text{and} \quad \nu = \frac{V_{inj}}{R} \omega_i^0 \end{aligned} \quad (3)$$

where  $\omega^0 = \omega_r^0 + i\omega_i^0$  and  $A$  represents the initial amplitude of the perturbation, an initially unknown value. There is no need to specify the initial amplitude  $A$  as long as  $q$  is a solution of a linear system.

Two major results stemming from the stability analysis can be immediately pointed out. First, we note that the spectrum is discrete. As such, only a discrete set of circular frequencies exists for which unstable disturbances/waves can develop from the main flow. Second, all of the eigenvalues  $\omega$  bear a negative imaginary part. This implies that all of the spatially unstable modes will be exponentially damped in time. Their associated eigenfunctions will, however, grow exponentially in the streamwise direction.

The spatial growth of the oscillations is illustrated in figures 1(b) and 2(b); these present the spatial evolution of the real part of the eigenfunctions  $\hat{u}_x$  and  $\hat{u}_r$  for the eigenvalue  $\omega^0 = 40.409 - 9.164i$  and  $X_e = 8$ . Without having been prescribed in the theory (see (1)), the three-dimensional plots clearly show a strong (exponential-like) amplification in the streamwise direction. Thus for a given eigenvalue, two counteracting mechanisms are seen to coexist : a temporal decay affecting the perturbations as time elapses and a spatial growth in the perturbed amplitudes as wave propagation intensifies in the longitudinal direction  $x$ .

### 2.4 Mode Dependence on Motor Length

So far, the character of the instability modes has provided a new physical understanding of the mechanisms that drive the thrust oscillations in solid rocket motors. As confirmed by [12], the frequency paths recovered in all subscale and full scale motors are caused by the emergence of the instability modes of the flow (also called intrinsic instabilities). The emergence is attributed to the coupling between the stability modes and the natural acoustic frequen-

cies of the motor. The instability modes are excited and then amplified by the acoustic sources. After inception, they undergo temporal depreciation as predicted theoretically. However, despite the new physical insight gained from linear stability analysis toward elucidating the origination of the thrust oscillations, a question remains unresolved. As one may infer from figure 3, the eigenvalues appear to depend on the length of the domain  $X_e$ . So by changing the length of the domain, a shift in complex eigenvalues is detected despite the invariance of the mean flow. Given no established explanation for such behavior, it may be speculated that the size dependence is a spurious artefact of the numerical procedure, thus calling into question the whole validity of the stability analysis. To better understand this sensitivity to  $X_e$ , an independent approach is resorted to, specifically, that of Direct Numerical Simulation (DNS). Consequently, besides the investigation of coupling mechanism, numerical simulation should first confirm this dependence on motor length.

### 3 DIRECT NUMERICAL SIMULATION

As alluded to earlier, we have performed extensive DNS computations with the use of ONERA's code known as CEDRE. The space discretization in CEDRE is based on a finite volume approach that employs an upwind Roe scheme with a second order extension (MUSCL scheme with Van Leer limiter). A complete description of the code is given by [13] and more specific information concerning code validation for rocket motor simulations may be found in a survey [14].

For the present study, laminar Navier-Stokes computations are carried out. In the interest of establishing realistic baseline computational cases, the characteristic length and velocity are chosen to match those of in the VALDO facility. So in the DNS input file, we use a chamber radius of  $R = R_0 = 0.03$  m and an injection velocity of  $V_{inj} = 1$  m/s.

Four meshes are successively tested to the extent of establishing grid independence. Our sample results for  $X_e = 8R$  are performed with a grid that is composed of  $301 \times 161$  nodes (for  $X_e = 10R$  the grid is composed of  $351 \times 161$  nodes such that the thickness of the cells at the headend is conserved compared to case  $X_e = 8R$ ). Furthermore, cosine repartition is employed such that the thickness of the cells on the boundaries is refined down to ap-

proximately  $3 \mu\text{m}$ . Note that as the considered values of  $X_e$  are small enough to maintain a laminar flow, 2D DNS computations can be performed without restrictions on the results except the axisymmetric property.

#### 3.1 Computing the Mean Flow

An implicit time scheme is used with a fixed value of the Courant-Friedrich-Levy (CFL) number. Using  $\text{CFL} = 10$ , steady-state runs are conducted for the purpose of computing the basic flow components that are needed for the linear stability calculations. While it is possible to use the Taylor-Culick approximation, we opt for the computed solution because of its ability to satisfy the headwall boundary condition. Once the computations are confirmed to have reached a converged state, the steady flow is retrieved in discrete fashion and put into the stability code, thus supplanting the Taylor-Culick formula.

In principle, a no-slip condition at  $x = 0$  is essential for a viscous fluid, a condition that is not observed by the Taylor-Culick profile. Nonetheless, the boundary layer that develops at  $x = 0$  only affects the flow in the vicinity of the headwall. In this neighborhood (see figures 1(b) and 2(b)), the fluctuations are nearly zero, and so the use of the Taylor-Culick solution continues to be a suitable approximation: it leads to practically identical stability results (in terms of circular frequency  $\omega_r$ ). For further detail on this issue, the reader may refer to [7].

#### 3.2 Unsteady Calculations

To compute the unsteady fields, an explicit time scheme is used with a time step of  $\Delta t = 5 \times 10^{-9}$  s. The corresponding maximum CFL number is less than 1. The objective is to reproduce the coupling between acoustic modes and intrinsic modes suspected to be responsible of the thrust oscillations.

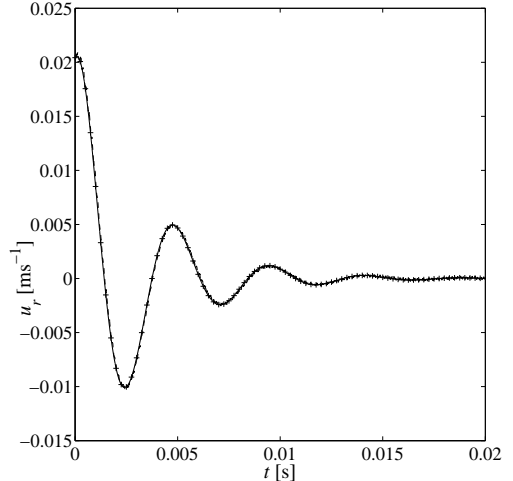
##### 3.2.1 Code validation

Before performing such a computation, a validation test case is chosen in order to check the ability of the CEDRE code to reproduce the behavior of an intrinsic instability. Thus, the strategy is to superimpose, at the initial time, an instability mode  $\omega = \omega^0$ , extracted for example from figures 1(b) and 2(b), where  $\omega^0 = 40.409 - 9.164i$ , on the DNS calculated basic flow, illustrated in figures 1(a) and 2(a). The initial time  $t$  and amplitude  $A$  of (3) are chosen as  $t = 0$  s and  $A = 0.01A_0$ , where  $A_0$  is the peak value

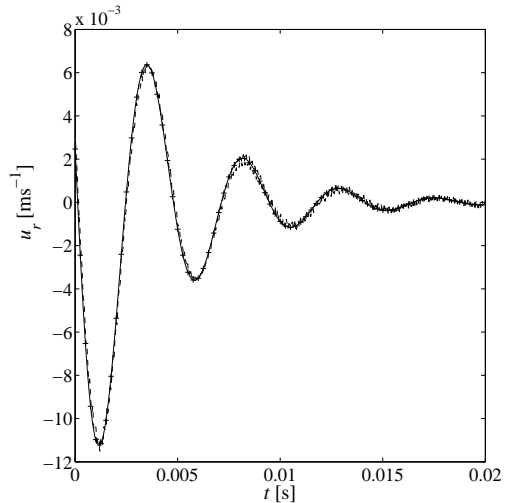
attained by the longitudinal component  $\bar{U}_x$  of the mean flow. It may be important to note that the pressure perturbation of the stability mode  $\omega = \omega^0$  is not superimposed on the pressure distribution of the mean flow, being very small in amplitude. At first glance, the superposition process may appear to be simple. In actuality, the overlapping of the mean and unsteady components proves to be quite challenging. It requires careful grid projections that do not introduce artificial errors. It also requires special attention to be paid to the boundary conditions. Once the superposition is resolved, the unsteady DNS computations are started. The origin of time is set at  $t = 0$  s. At  $t = 0.02$  s, that is to say after 4,000,000 iterations, our computer runs are stopped and their output exported. Signals from different virtual sensors are extruded and analyzed. As the purpose of this paper is not addressed to code validation, only a few results will be given here. A complete description of different test cases can be found in [15] and [16]. To illustrate the results produced by our numerical strategy, two cases are retained. Case 1 corresponds to the superposition of eigenmode  $\omega^0 = 40.409 - 9.164i$  in a chamber length  $X_e = 8R = 0.24$  m whereas case 2 corresponds to the superposition of eigenmode  $\omega^0 = 40.367 - 7.302i$  in a chamber length  $X_e = 10R = 0.3$  m, see 3. Figures 4(a) and 4(b) present comparisons between signals from specific sensors located inside the chambers and the theoretical evolution given by (3). These figures clearly demonstrates the ability of the CEDRE code to simulate the evolution of eigenmodes. In fact, only the modes shapes are introduced at  $t = 0$  in the computation, the circular frequency and the temporal damping being not prescribed. The observed perfect matchings also confirms the mode dependance on the motor's length  $X_e$ , see paragraph 2.4.

### 3.2.2 Simulating the coupling between acoustic modes and eigenmodes

Now that the code has been validated for eigenmodes simulations, one can consider simulating coupling with acoustic modes. The idea is to reproduce the crossing of the frequencies of an acoustic modes and an eigenmode. As the frequency of an acoustic mode is only depending on the motor length  $X_e$  whereas an eigenmode one depends on the ratio  $\frac{V_{inj}}{R}$ , the easiest way to achieve our goal is to use unsteady boundary conditions. The



(a)  $u_r$  at  $(x, r) = (7.333R, 0.342R)$  for case 1



(b)  $u_r$  at  $(x, r) = (8R, 0.809R)$  for case 2

Figure 4: Comparisons between the fluctuating part of the signal issued from virtual sensors (dashed line) and the theoretical evolutions (solid line with +) given by (3).

domain length  $X_e$  and the radius  $R$  will be fixed, while the spatially constant injection velocity  $V_{inj}$ , imposed on the lateral wall, will range linearly from 0.98 m/s to 1.02 m/s during the computation. With these values, the frequency of the eigenmode  $\omega = 68.679 - 7.594i$  is expected to evolve from 357 Hz to 371 Hz. For  $X_e = 8R = 0.24$  m, the frequency of the first acoustic mode is 363 Hz. Thus, using an unsteady injection velocity, the desired frequency crossing will happen as it happens during a live solid rocket motor firing because of the propellant regression. Considering a time step of  $\Delta t = 5 \times 10^{-9}$  s and a final time  $t = 0.08$  s (16,000,000 iterations), the frequency variation speed for the eigenmode is about 180 Hz/s. In a similar configuration, the expected coupling has been observed in the VALDO facility but for a variation speed of 30 Hz/s. One can fear that such a high variation speed compromises the coupling effectiveness.

An other issue concerns the existence of eigenmodes in the computations. To simulate the coupling with an acoustic mode, the eigenmode  $\omega = 68.679 - 7.594i$  must be present in the simulation. As explained earlier, these eigenmodes are temporally stable and so they need to be excited to exist. A continuous noise in the computation can allow the existence of several eigenmodes at low amplitude levels without leading to the amplification of a particular eigenmode which would prevent the expected coupling. To do so, a small mesh distortion is introduced at the injection wall. The mesh distortion associated with a wall normal injection boundary condition will create an injection noise suitable for exciting several eigenmodes.

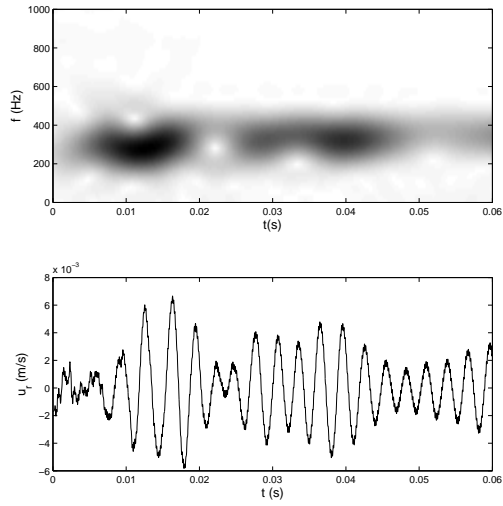
An initial harmonic distribution of the first ten acoustic modes is superimposed to the mean flow calculated for the fixed injection velocity value  $V_{inj} = 0.98$  m/s. More precisely, only the pressure distribution is superimposed to the mean flow with an amplitude of  $0.001P_{atm}$ ,  $P_{atm}$  being the atmospheric pressure imposed at the exit  $x = X_e$ . Finally, the computation is started from this superimposition and stopped after only 12,000,000 iterations. At a first glance, the results appear to be mainly composed by noise. In fact, all the signal  $u_x$ ,  $u_r$  or  $p$  for the whole set of sensors exhibit the same amplified frequency  $f = 6050$  Hz. A more careful analysis revealed a behavior similar to an intrinsic instability but without any interest regarding our goal. To eliminate this frequency, the signals are filtered thanks to a Butterworth filter of order 5 with a cutting frequency  $f_c = 2000$  Hz. In addition, the continuous part of

the signals has been removed in order to avoid accuracy problem in the low frequency range during the later time-frequency analysis. Note that the continuous part is only linked to the linear evolution of the injection velocity  $V_{inj}$ . Short Time Fourier Transforms (STFT) are performed on different sensor signals.

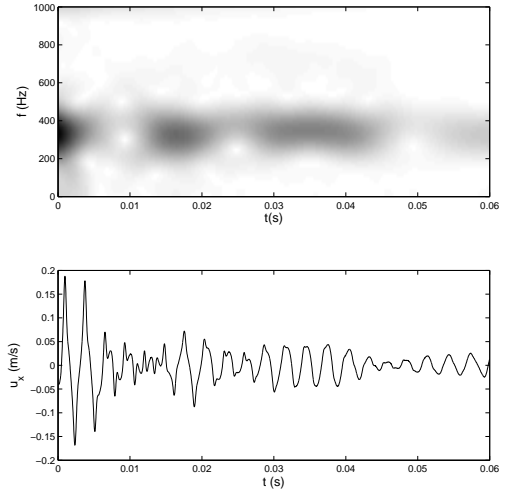
Figures 5(a) and 5(b) provide the results obtained from radial velocity signals for two different sensors locations \*. It is interesting to focus on the radial velocity component, because the possible fluctuations that can exist can only be attributed to the emergence of an eigenmode. In fact, the acoustic radial velocity in such a configuration is almost zero as the Mach number is low, see [17]. The figures clearly show the emergence of two distinguished eigenmodes. Around  $t = 0.03$  s, one observed the expected emergence of eigenmode  $\omega = 68.679 - 7.594i$ . The frequency crossing has led to the growing of this eigenmode, thus confirming the existence of coupling mechanism between acoustic modes and intrinsic instabilities. Note that the emergence happened earlier in the computation compared to the theoretically expected time  $t = 0.04$  s. The presence of noise may have slightly affected the mean flow and thus modified its intrinsic instabilities.

In addition to the desired amplification of eigenmode  $\omega = 68.679 - 7.594i$ , one observes a previous amplification corresponding to the circular frequency  $\omega = 62$  close to those of the neighboring eigenmode, see 3. The reason of this emergence is not clear. To learn more about it, and also to confirm the emergence of eigenmode  $\omega = 68.679 - 7.594i$ , figures 6(a) and 6(b) give the results obtained for the axial velocity component and the pressure signals of a specific sensor. The emergence of eigenmode  $\omega = 68.679 - 7.594i$  is retrieved. The signal of figure 6(a) suggests that the first amplification also implies the first acoustic mode. In fact, the shape of the signal resembles the acoustic signature that can be seen at the very beginning of the simulation. Up to now, there is no clear explanation for this amplified part of the signal. Non linearity can be involved in this observation.

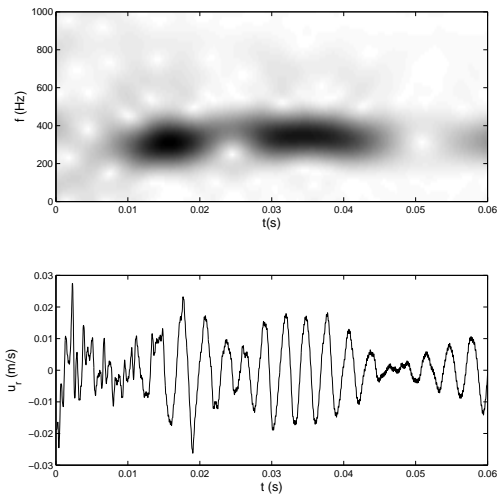
\*Because the eigenmodes are exponentially amplified in the  $x$  direction, significant amplitudes are only reached near the exit section. For clarity reasons, it is thus preferable to present the results extracted from sensors signals located in this area.



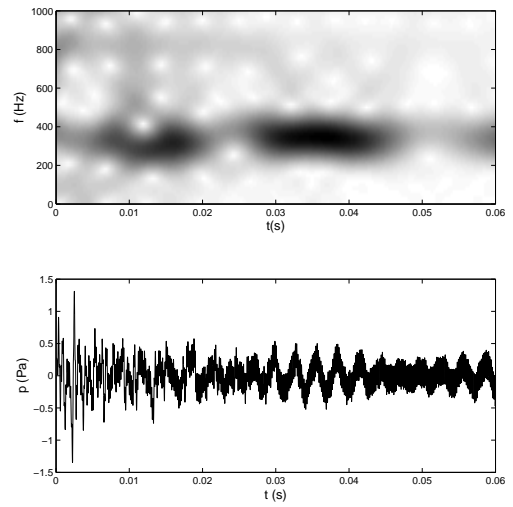
(a)  $u_r$  at  $(x, r) = (7.222R, 0.309R)$



(a)  $u_x$  at  $(x, r) = (8R, 0.809R)$



(b)  $u_r$  at  $(x, r) = (8R, 0.809R)$



(b)  $p$  at  $(x, r) = (8R, 0.809R)$

Figure 5: Radial velocity component signals (down) of two virtual sensors and the respective STFT (up)

Figure 6: Axial velocity component and pressure signals (down) of a virtual sensor and the respective STFT (up)

## 4 CONCLUSION

In this paper, DNS computations showing the possible existence of a coupling between acoustic and intrinsic modes in a solid rocket motor have been presented. This major result confirms the assumptions sprang from the linear stability theory results. When an eigenmode fall close to a natural frequency of the motor, a significant amplification is noted that can lead to appreciable wave steepening. Conversely, when the eigenmode is sufficiently spaced from the chamber's natural frequencies, no appreciable amplification is seen. After a short growing phase, the eigenmode is then damped with the passage of time. This behavior is illustrated on figure 3.2.2 for firing 24 of the so-called subscale motor LP9 [3]. The amplifications of intrinsic insta-

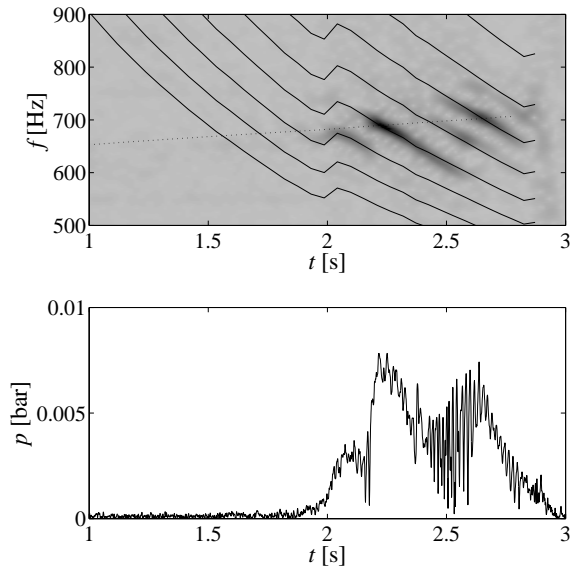


Figure 7: Pressure signal (bottom) and its STFT (top) of firing 24 of subscale motor LP9. The eigenmode frequencies are reported on the STFT as solid lines whereas the first longitudinal acoustic mode one is drawn as a dotted line.

bilities, due to the frequency crossing with the first longitudinal acoustic mode, are clearly visible. The measured amplifications of the pressure signal correspond to the eigenmode frequencies which are ruled by the ratio  $\frac{V_{inj}}{R}$ . Note that several amplifications coexist, implying several different modes and thus confirming the implication of the intrinsic instabilities.

Consequently, a consistent scenario is now available for explaining the occurrence of the thrust oscillations in a solid rocket motor. Further numerical simulations may solve the remaining questions such as the coupling mechanism in order to find out a possible way to control the thrust oscillations.

## 5 ACKNOWLEDGMENT

This study has been supported by the French Space Agency CNES and by ONERA. The authors thank M. Prévost and G. Avalon from ONERA for their accurate measurements, help, and useful suggestions.

## References

- [1] Chedevergne, F., Casalis, G., and Féraïlle, T., "Biglobal Linear Stability Analysis of the Flow Induced by Wall Injection," *Physics of Fluids*, Vol. 18, No. 1, 2006, pp. 014103–14.
- [2] Chedevergne, F. and Casalis, G., "Thrust Oscillations in Reduced Scale Solid Rocket Motors, Part II : a Theoretical Approach," *AIAA Paper 2005-4000*, July 2005.
- [3] Prévost, M. and Godon, J.-C., "Thrust Oscillations in Reduced Scale Solid Rocket Motors, Part I : Experimental Investigations," *AIAA Paper 2005-4003*, July 2005.
- [4] Avalon, G. and Lambert, D., "Campagne d'essais VALDO, periode 2000/2001," Tech. Rep. RT 2/05424 DEFA, ONERA, Etablissement de Palaiseau, octobre 2001.
- [5] Taylor, G. I., "Fluid Flow in Regions Bounded by Porous Surfaces," *Proceedings of the Royal Society, London, Series A*, Vol. 234, No. 1199, 1956, pp. 456–475.
- [6] Culick, F., "Rotational Axisymmetric Mean Flow and Damping of Acoustic Waves in a Solid Propellant Rocket," *AIAA Journal*, Vol. 4, No. 8, 1966, pp. 1462–1464.
- [7] Chedevergne, F. and Casalis, G., "Front Wall Boundary Layer Influence on the Stability of the Flow Induced by Wall Injection," *7<sup>th</sup> ONERA DLR Aerospace Symposium*, Toulouse, France, 4-6 October 2006.
- [8] Majdalani, J., "On Steady Rotational High Speed Flows : the Compressible Taylor-Culick Profile," *Proceedings of the Royal So-*

*ciety, London, Series A*, Vol. 463, No. 2077, 2007, pp. 131–162.

- [9] Theofilis, V., “Advances in Global Linear Instability Analysis of Nonparallel and Three-Dimensional Flows,” *Progress in Aerospace Sciences*, Vol. 39, No. 2, 2003, pp. 249–315.
- [10] Casalis, G., Chedevergne, F., Féraïlle, T., and Avalon, G., “Global Stability of the Flow Induced by Wall Injection,” *IUTAM, Symposium on Laminar-Turbulent Transition*, Bangalore, India, December, 13-17 2004.
- [11] Golub, G. and Loan, C. V., *Matrix Computations (Third Edition)*, The Johns Hopkins University Press, 1996.
- [12] Chedevergne, F. and Casalis, G., “Detailed Analysis of the Thrust Oscillations in Reduced Scale Solid Rocket Motors,” *AIAA Paper 2006-4424*, 2006.
- [13] Chevalier, P., Courbet, B., Dutoya, D., Klotz, P., Ruiz, E., Troyes, J., and Villedieu, P., “CEDRE : Development and Validation of a Multiphysic Computational Software,” *1st European Conference for Aerospace Sciences (EUCASS)*, Moscow, Russia, 2005.
- [14] Vuillot, F., Scherrer, D., and Habiballah, M., “CFD Code Validation for Space Propulsion Applications,” *5th International Symposium on Liquid Space Propulsion*, Chattanooga, Tennessee, 2003.
- [15] Chedevergne, F., Casalis, G., and Majdalani, J., “DNS investigation for the Taylor-Culick flow stability Analysis,” *43<sup>rd</sup> AIAA/ASME/SAE/ASEE Joint Propulsion Conference and Exhibit*, Cincinnati, Ohio, 8-11 July 2007.
- [16] Chedevergne, F. and Casalis, G., “Biglobal linear stability analysis and DNS investigation of the flow induced by wall injection,” *6<sup>th</sup> ERCOFTAC SIG 33 workshop*, Kleinwalsertal, 8-11 June 2007.
- [17] Flandro, G. A. and Majdalani, J., “Aeroacoustic Instability in Rockets,” *AIAA Journal*, Vol. 41, No. 3, March 2003, pp. 485–497.